

Compressible Boundary-Layer Transition on an Axisymmetric Body at Incidence

Hiroki Sugiura*, Naoko Tokugawa† and Yoshine Ueda‡
 Japanese Aerospace Exploration Agency, Chofu, Tokyo 182-8522, Japan

Experimental investigation of the boundary-layer transition on an axisymmetric nose model at 1- and 2-deg incidence was conducted at Mach 1.2. The configuration of the model is the forward part of a Sears-Haack body defined to have minimum wave drag due to volume at 0-deg incidence in supersonic flow. Transition locations were obtained with small surface roughness on the order of 0.1 micron using an infrared camera. An unsteady pressure transducer was applied to investigate instability mechanisms that lead to transition. These results show that the most aft transition occurred on the leeward ray rather than on the windward rays as observed on sharp cones. Tollmien-Schlichting instability dominated the transition process on the windward ray and crossflow instability was assumed to dominate on the side similar to the transition on the sharp cones. However, transition occurred more aft on the leeward ray than for the case of the sharp cones and the transition front was determined by turbulent wedges formed as a consequence of the more forward transition on the side. The disturbance believed to be a traveling crossflow wave was observed at 1-deg incidence and its measured frequency was in good agreement with the maximum amplified frequency, which was calculated using a compressible linear e^N code.

Nomenclature

C_p	pressure coefficient
M	Mach number
P	pressure
P'	pressure fluctuation
Re	Reynolds number
T	temperature
Tu	freestream turbulence
x	distance measured axially from cone apex
α	angle of attack, deg
γ	intermittency factor
θ	meridian angle measured from leeward ray
<i>Subscripts</i>	
0	freestream stagnation condition
rms	root-mean-square average
unit	unit

Introduction

Friction drag makes up more than one-third of the drag of next-generation supersonic transports (SST) and its reduction by delaying boundary-layer transition remains an attractive and effective measure for improving the lift-to-drag ratio. Achievement of laminar flow for up to 60% of wing chord for a next-generation supersonic transport configuration has been estimated to produce a total-aircraft drag reduction of 14%¹.

The flowfield over aircraft is, however, generally fully three-dimensional (3D) and an understanding of 3D

boundary-layer transition is critical for delaying the transition. Although many issues remain unsettled in incompressible 3D boundary layers, the present investigation is part of a project that begins serious study of transition mechanisms in supersonic 3D boundary layers, which are more relevant to supersonic flight.

The simplest geometries that exhibit 3D supersonic boundary layers are round cones at angle of attack (AOA) and elliptic cones². Round cones are useful in that two-dimensional flow is realized at zero AOA and varying the AOA can easily control three-dimensionality.

Thus, a number of experiments have been conducted to investigate the transition for round cones at incidence³⁻⁶. The previous studies have consistently found that as the AOA is increased, transition moves rearward on the windward ray and forward on the leeward side³⁻⁶. Stability experiments⁷⁻⁸ showed that Tollmien-Schlichting (T-S) instability dominates the transition process on the windward ray. Observations of streamwise vortices^{3, 9-10} revealed that crossflow (C-F) instability dominates on the side. Boundary-layer-profile measurements⁷⁻⁸ showed that flow profiles along the leeward ray are highly inflectional.

There is little pressure gradient on sharp cones and no pressure gradient exists on their leeward and windward rays (Fig. 1). However, the question remains: "What occurs with large pressure gradients, such as in noses and wings of aircraft?" All the previous studies of transition on axisymmetric bodies at incidence¹¹⁻¹² are restricted to subsonic speed except for those on cones.

It is unknown whether inflectional profile on the leeward ray exists in the presence of a large pressure gradient. Since favorable pressure gradients stabilize T-S

*Researcher, Aerodynamics Research Group, Senior Member AIAA.

†Senior Researcher, Aerodynamics Research Group.

‡Researcher, Information Technology Center.

SUGIURA 2004

NICE
 travel (Kash)
 SPS trans. content

instabilities and amplify C-F instabilities on the side, the transition front moves rearward on the windward ray and may move forward on the side. The difference in transition location may become sufficiently large so that the transition on the windward ray might be affected by the early transition on the side.

The surface painted with an oil film, temperature sensitive paints, liquid crystals etc. are not suitable for studying the crossflow-induced transition, which is influenced by submicron surface roughness¹³. The present study uses an infrared (IR) camera to acquire the transition front with little influence of surface roughness.

The purposes of this paper are to:

1. Compare the 3D boundary-layer transition with and without large pressure gradients.
2. Investigate the underlying stability mechanisms determining transition location.

Experimental Procedure

Test Model

We used an axisymmetric nose model that is 700 mm long measured axially from apex to base (Fig. 2). The model is a 23.4% scale model of the nose of a non-powered experimental supersonic transport airplane (NEXST-1) that was developed at Japan Aerospace Exploration Agency (JAXA). The configuration of the nose is the forward part of a Sears-Haack body defined to have minimum wave drag due to volume at zero AOA (Fig. 1b). The Sears-Haack body serves as a guideline reference for designing fuselages of supersonic aircraft.

The model is made of insulated material so that surface temperature distribution can be acquired by an IR camera. The IR camera technique usually requires the use of adiabatic material to maintain the differences in wall temperature.

Use of resin with high processability allows us to attain the transition front with little influence of surface roughness. Thus, the model is made of an amorphous fiber reinforced plastic called polysulfone. The RMS amplitude of the roughness of the model is 0.22 μm . No bluntness effect exists on the model since its geometry is defined to be blunt.

An unsteady pressure transducer is installed at $x=620$ mm location on the model and static pressure fluctuation can be measured on the surface. By varying the roll angle of the model, circumferential distribution of the fluctuation can be obtained. The pressure transducer is 1.6 mm in diameter and is mounted flush with the model surface. No level difference was identified through examination by touch and was confirmed with a thickness gage to be below 50 μm .

For static pressure measurements, we used another model with the same configuration. The model has 6

static ports.

Test Facility

The experiment was conducted in the 2×2 m transonic wind tunnel of JAXA in Japan.

The static pressure fluctuation normalized by dynamic pressure C_{Prms} at $M=1.2$ was 0.34% in the tunnel, which was measured with bandwidth from 25 Hz to 20 kHz (Ref. 14). The tunnel was the available transonic tunnel with the lowest turbulence level. However, without such care as taken in the quiet tunnels, the tunnel-wall boundary layer is apparently turbulent. Fig. 3 shows the power spectrum of the static pressure fluctuation on a 10-deg cone at $M=1.2$ measured by Oguni et al.¹⁴. There is no particular frequency dependency in the fluctuation. Fig. 4b shows the power spectrum of the static pressure fluctuation of a laminar boundary layer on the present model at 0-deg AOA and $M=1.2$ measured with bandwidth from 125 Hz to 100 kHz. This power spectrum shows that the pressure fluctuation is at lower level above 20 kHz than below 20 kHz.

Varying the total pressure can control unit Reynolds number. Fig. 4a and 4b show the effect of total pressure on the surface pressure fluctuation and its spectral content, respectively, at 0-deg AOA and $M=1.2$. It is clear that the total pressure has little effect on the pressure fluctuation and its spectral content so that by varying the total pressure of the tunnel from 50 to 70 kPa, the unit Reynolds number effect on the transition can be studied.

Measurement Technique

Infrared Camera

We used an 12-bit IR camera to map the transition front with little influence of surface roughness. In order to acquire full surface distribution of the transition front, the camera was placed in two different positions as shown in Fig. 5 and IR images were taken from three sides. The bottom view of the model at a positive incidence was taken by setting negative incidence of the same magnitude.

Since the camera was placed inside the plenum chamber where the static pressure is 20.6 kPa at $M=1.2$, it was installed in an atmospheric pressure chamber.

IR camera technique is based on measurements detecting variable wall temperatures in the transition region due to different recovery temperatures of laminar and turbulent flows.

Fig. 11a shows a raw IR image acquired at 0-deg AOA. The circumferential temperature distribution of its profile is shown in Fig. 6. The position of the profile is shown as a straight line in the Fig. 11a. Here, ϕ is defined as a cone meridian angle measured from the intersection line of the model surface and the plane defined by the

center axis of the model and the focal point of the camera. The Fig. 6 shows that the IR signal is constant with a scatter within $\pm 0.1K$ in the range of $|\phi| < 82$ deg and degrades in the peripheral area. A measurement of optic-angle dependency of the temperature measured using this camera¹⁵ was carried out for a variable-angle flat plate whose temperature is kept constant using a thermostat. The measurement showed that the measured temperatures at 70- and 75-deg optic angle were 95 and 93% of those at 0-deg optic angle, respectively. Thus, every data analysis was made in the range of $|\phi| < 75$ deg.

Distortion and aeroelastic deformation were corrected by 3D affine transformation. The actual coordinates of the model were measured at no-wind condition by putting markers made of aluminum tape on the model surface.

Fig. 7 shows two typical temperature profiles along the streamlines calculated using a 3D Navier-Stokes (N-S) code. This code uses the Baldwin-Lomax model and was previously validated by experiments and other numerical codes¹⁶. The temperature remains constant when the flow is either laminar or turbulent and changes linearly with distance during the transition. Thus, the beginning of the transition was defined as the location of the intersection point of two approximate lines of least squares respectively through the laminar and turbulent region. The beginning of transition corresponds to the boundary line between the light and dark blue regions.

The accuracy of the location of the beginning of transition obtained using the IR camera is estimated to be 1%. The estimation is based on the image length of 1.2 mm corresponding to one pixel and temperature resolution of 0.08K. Temperature resolution of the infrared camera was 0.08 K and was very small compared to our observed differences between surface temperature of laminar and turbulent boundary layer which were in the 3-4 K range.

Unsteady Pressure Transducer

We also used the unsteady pressure transducer (Kulite XCQ062) to investigate the nature of the disturbance present at the initial stage of transition.

The propriety of the use of unsteady pressure transducer for the disturbance measurement must be considered. From the one-dimensional isentropic relations,

$$p + \rho u^2 = \text{const.} \quad (1)$$

Writing each quantity as the instantaneous deviations of a fluctuating quantity with reference to its temporal mean value gives

$$p = \bar{p} + p', \quad u = \bar{u} + u', \quad \rho u = \bar{\rho u} + (\rho u)'. \quad (2)$$

Eq. (1) is then equivalent to

$$\frac{p'}{\bar{p}} = \gamma M^2 \left(\frac{(\rho u)'}{\bar{\rho u}} + \frac{u'}{\bar{u}} \right). \quad (3)$$

Hence, pressure fluctuation is proportional to a sum of mass flow fluctuation and velocity fluctuation.

The pressure fluctuation was measured with bandwidth from 125 Hz to 100 kHz.

Correlation of data against unit Reynolds number using both measurement techniques is given in Fig. 8. The location of the fluctuation and surface temperature data is fixed at $x=620$ mm station and the total pressure of the flow is varied. The pressure fluctuation data clearly show a rise from the laminar to turbulent level with an intermediate peak. The rise in the fluctuation data takes place at lower Reynolds number than for the beginning of transition defined by IR data. This is apparently because a change in a fluctuating quantity occurs earlier than a change in a mean-flow quantity such as surface temperature. Note that location of peak fluctuation coincides with the maximum surface temperature location. It has been established by Owen¹⁷ that the location of peak voltage fluctuation determined using hot-film sensors on a surface coincides with the maximum burst frequency location and the maximum surface temperature location. Accordingly, peak location of the pressure and the hot-film voltage fluctuation coincides; this proves the consistency of the present stability measurement by the pressure transducer.

The intermittency factor was calculated from the pressure fluctuation data by the method proposed by Townsend¹⁸. Kurtosis is calculated from measurements of the flattening factors, assuming that the flattening factors taken only during periods of turbulent flow are identical with those observed in fully turbulent flow where experiment in isotropic turbulence has shown that

$$\frac{\overline{u^4}}{(\overline{u^2})^2} = \frac{\overline{v^4}}{(\overline{v^2})^2} = \frac{\overline{w^4}}{(\overline{w^2})^2} = 3.00 \quad (4)$$

Then, intermittency factor is

$$\gamma = 3.0 \frac{(\overline{u^2})^2}{\overline{u^4}} = 3.0 \frac{(\overline{v^2})^2}{\overline{v^4}} = 3.0 \frac{(\overline{w^2})^2}{\overline{w^4}} \quad (5)$$

Based on Eq. (3), we assume that the following relation can be used for the pressure fluctuation.

$$\gamma = 3.0 \frac{(\overline{p^2})^2}{\overline{p^4}} \quad (6)$$

The assumption is justified by the consistency of values of γ measured in this way (Fig. 9).

The accuracy of the pressure fluctuation is estimated to be 2%. The estimation is based on the diameter of the transducer, 1.6 mm, resolution of 0.1%, and an assumed estimation error of 1.5% in the process of static pressure calibration.

Results and Discussion

Surface Pressure Distributions

Comparisons between the measured and calculated pressure distributions along streamlines on the model at 1- and 2-deg AOA are shown in Fig. 10. The pressure transducer fixed at $x=0.62\text{m}$ lies on the streamline labeled "side" in the figures, when the transducer is set at $\theta=90$ deg. Here, θ is defined as a cone meridian angle measured from the leeward ray. The streamlines and the calculated pressure distributions were obtained with the same 3D N-S code used in the previous chapter. The agreement between the measurements and the computation is very good. Large favorable pressure gradients exist on the model at every AOA. Note that at each AOA the smallest maximum pressure gradient is achieved on the windward ray and that the gradient on the leeward ray is greater.

Distributions of Transition Fronts

Fig. 11b, 11c and 11d show top, side and bottom views of surface temperature distribution of the model at 2-deg AOA, respectively, determined using the IR camera. Fig. 11e, 11f and 11g show the top, side and bottom views at 1-deg AOA, respectively. As stated above, the transition front corresponds to the boundary line between light and dark blue regions. The foremost transition occurred at $\theta=90$ deg at each AOA. It is noteworthy that the transition occurred more aft on the leeward ray than on the windward ray at each AOA; the most aft transition occurred on the leeward ray.

Overall, the shapes of the transition front are similar at both AOA. However, note that the shapes of the transition front near the leeward ray are different; an angle determined by the transition front is acute at 2-deg AOA but is obtuse at 1-deg AOA.

The previous studies on the cones have consistently found that the transition front moves monotonically forward between the windward and the leeward ray³⁻⁶. As on the cones, in the range from $\theta=90$ to 180 deg, the measurements show the transition point moving rearward with increasing θ . A unique feature of the present model is that the most aft transition occurred on the leeward rays rather than on the windward rays as observed on the cones.

As stated above, the maximum pressure gradient was smaller on the windward ray than on the leeward ray at each AOA; this may account for the more aft transition point on the leeward ray rather than on the windward ray. However, since different instability mechanisms may be responsible for transition on both rays, this will be discussed further in the following chapter.

The smallest maximum pressure gradient was achieved on the windward ray. Accordingly, from $\theta=50$ to 150 deg, the transition occurred more forward from $\theta=50$ to 150 deg than $\theta=180$ deg despite of the larger

pressure gradient. Since the favorable pressure gradient amplifies C-F instabilities but stabilizes T-S instabilities, this implies that C-F instability dominates the transition. However, additional measurements are needed for justification. Since the foremost transition occurred at $\theta=90$ deg, let us concentrate our attention on this angle.

Thus, to identify instability mechanisms at $\theta=90$ deg, and on the windward and leeward rays, we carried out additional measurements using the unsteady pressure transducer.

Boundary-Layer Disturbance Spectra

Fig. 12a shows the effect of total pressure on power spectrum at a point at $x=0.62$ m at 0-deg AOA. Significant disturbance growth is clearly observed in the 10-20 kHz frequency band, with peak amplitude at 16 kHz. The maximum amplified frequency calculated using a compressible e^N code with an envelope method strategy is also plotted in the figure. In the calculation, compressible laminar boundary-layer profiles were calculated using a 3-D N-S code with 70 grid points in the boundary layer. The profiles were validated using an axisymmetric laminar boundary-layer code¹⁰ based on the methods developed by Kaups and Cebeci. Nonparallel and curvature effects are not included in the present code. The e^N code is validated experimentally and using another linear stability code¹⁹ developed by Arnal et al. based on the envelope method. The calculated frequency and the measured peak frequency are in good agreement.

Fig. 12b shows the effect of total pressure on power spectrum at $x=0.62$ m on the windward ray at 2-deg AOA, together with a calculated maximum-amplified frequency. Significant disturbance growth is clearly observed in the 10-20 kHz frequency band, with peak amplitude at 16 kHz. The calculated frequency and the measured peak frequency are in good agreement. According to the calculation, crossflow velocity components were zero along the windward ray. Therefore, we can be fairly certain that T-S instability dominates the transition. As for the cones, T-S instability also dominates on the leeward ray according to the stability measurements⁷⁻⁸. Hence, the stability mechanism on the leeward ray does not change in the presence of the large pressure gradient.

Fig. 12c shows the effect of total pressure on power spectrum at $x=0.62$ m on the leeward ray at 2-deg AOA. Note that fluctuations of all frequencies grow monotonically and that there is clearly no frequency dependency despite measurement with minute 2-3 kPa steps in total pressure.

Fig. 14 shows the effect of total pressure on the magnitude of the pressure fluctuation. The value at

$P_0=50$ kPa is 2 dB lower on the leeward ray than on the windward ray. Moreover, Fig. 12c shows that the spectrum at $P_0=50$ kPa coincides with that on the windward ray at $P_0=50$ kPa shown in Fig. 12b which is apparently laminar. These things suggest that the boundary layer is laminar on the leeward ray at $P_0=50$ kPa.

Intermittency factors are also plotted in the Fig. 14. There is a clear relationship between the magnitude of the pressure fluctuation and the intermittency factor of the signal. This relationship suggests that the rise in the pressure fluctuation is due to increase in the intermittency of the flow. Fig. 15 shows the time-coordinate output signals of the unsteady pressure transducer. Burst-like signal is observed at total pressures above 64 kPa.

The angle between the transition front and each streamline is 9 deg, which lies in the range of 8-11 deg of half-apex angle of turbulent wedge²⁰. All these things make it clear that the acute angle of the transition front was determined by turbulent wedges formed as a consequence of the more forward transition on the side.

Fig. 12d shows the effect of total pressure on power spectrum at $x=0.62$ m on the leeward ray at 1-deg AOA. The calculated frequency and the measured peak frequency are in good agreement. Therefore, the disturbance is assumed to be T-S wave. Thus, the difference of the angles of the transition front near the leeward ray can be attributed to whether the transition on the side occurs sufficiently forward. Accordingly, it is likely that at 2-deg AOA, without the influence of the transition on the side, the transition is dominated by T-S instability and the transition point moves further rearward. As for the cones, flow profiles along the leeward ray are highly inflectional according to the profile measurements⁷⁻⁸. Hence, in the presence of the large pressure gradient, inflectional profile does not seem to exist on the leeward rays.

Since at 2-deg AOA the flow is turbulent at $x=0.62$ m and $\theta=90$ deg even at the least attainable Reynolds number, let us concentrate our attention on the measurement at 1-deg AOA. Fig. 13 shows an enlarged view of surface temperature distribution around $x=0.62$ m and $\theta=90$ deg at 1-deg AOA. Stationary crossflow vortices are evident in the figure as light-dark patterns. The spacing of the vortices is 12 mm. The calculated wavelength of the crossflow wave is 12.1 mm and is in good agreement with the measured spacing. As stated above, the transition occurred more forward than on the windward ray in the presence of the larger pressure gradient which amplifies C-F instabilities but stabilizes T-S instabilities. From these observations, we assume that C-F instability dominates the transition at $\theta=90$ deg.

As for the cones, crossflow instabilities dominate on the side according to the several observations of streamwise vortices^{3,9-10}. Hence, in the presence of the large pressure gradient, the stability mechanism on the side does not change but affects the transition near the leeward ray.

Fig. 12e shows the power spectrum at $x=0.62$ m and $\theta=90$ deg at 1-deg AOA. Disturbance growth is clearly observed in the 6-15 kHz frequency band, with peak amplitude at 11 kHz. Note that the amplitude is smaller than on the windward rays. The calculated frequency and the measured peak frequency are in good agreement. However, the agreement is open to question because the envelope method assumes that a crossflow wave can suddenly change to a streamwise wave. The calculated frequency of the T-S wave on the windward and leeward ray are 14 and 8.4 kHz, respectively and both frequencies are different from this value. Thus, the observed disturbance does not originate in either ray. Several observations in the last few paragraphs imply that the disturbance is C-F traveling wave mode. Measurement by Bippes et al.²¹ indicated that traveling wave rather than stationary mode is dominant in high-turbulence environment of the order of $Tu=0.30\%$ and vice versa in low-turbulence environment ($Tu=0.05\%$). Hence, the traveling wave seems to be observed because of the high-turbulence environment ($C_{Prms}=0.34\%$).

Concluding Remarks

Boundary-layer transition on the forward part of a Sears-Haack body at 1- and 2-deg incidence was investigated at Mach 1.2. Surface roughness was 0.22 μ m rms. The static pressure fluctuation normalized by dynamic pressure C_{Prms} was 0.34% and the spectral content of the pressure fluctuation was fully documented.

Tollmien-Schlichting instability dominated the transition process on the windward ray similar to the transition on sharp cones.

The most aft transition at each AOA occurred on the leeward ray rather than on the windward rays as observed on the sharp cones. Inflectional profile does not seem to exist on the leeward rays, which was not similar to the sharp cones. At 2-deg AOA, the transition front near the leeward ray was determined by turbulent wedges formed as a consequence of the more forward transition on the side.

The foremost transition occurred at $\theta=90$ deg. Crossflow instability was assumed to dominate on the side similar to the transition on the cones. Stationary crossflow vortices were evident in the surface temperature distribution obtained with IR camera. The disturbance believed to be a traveling crossflow wave

was observed at 1-deg incidence. This seemed to be due to the high-turbulence environment.

Acknowledgements

The authors wish to acknowledge the help and advice received from Dr. Akira Nishizawa and Dr. Kenji Yoshida of JAXA. We also wish to thank Mr. Tadao Koyama who developed the whole IR camera system used in this research, Dr. Koji Izumi and Dr. Shohei Takagi of JAXA for their advice and encouragement.

References

- ¹Ueda, Y., and Yoshida, K., "Numerical Study on Optimum Pressure Distribution for Supersonic Natural Laminar Flow Design," *Proceedings of the 32nd Fluid Dynamics Conference*, Fukuoka, Japan, 2000 (in Japanese).
- ²Schmisseur, J. D., Schneider, S. P., and Collicott, S. H., "Receptivity of the Mach-4 Boundary-Layer on an Elliptic Cone to Laser-Generated Localized Freestream Perturbations," AIAA Paper 98-0532, 1998.
- ³King, R. A., "Three-Dimensional Boundary-Layer Transition on a Cone at Mach 3.5," *Experiment in Fluids*, Vol. 13, 1992, pp. 305-314.
- ⁴Stetson, K. F., "Mach 6 Experiments of Transition on a Cone at Angles of Attack," *Journal of Spacecraft*, Vol. 19, No. 5, 1982, pp. 397-403.
- ⁵Krogmann, P., "An Experimental Study of Boundary Layer Transition on a Slender Cone at Mach 5," AGARD CP 224, AGARD Symposium of Laminar-Turbulent Transition, Copenhagen, Denmark, 1977.
- ⁶Reda, D.C., "Boundary Layer Transition Experiments on Sharp, Slender Cone at Mach 5," AIAA Paper 78-1129, 1978.
- ⁷Doggett, G. P., Chokani, N., and Wilkinson, S. P., "Effect of Angle of Attack on Hypersonic Boundary-Layer Stability," *AIAA Journal*, Vol. 35, No. 3, 1997, pp. 464-470.
- ⁸Ladon, D. W., and Schneider, S. P., "Measurements of Controlled Wave Packets at Mach 4 on a Cone at Angle of Attack," AIAA paper 98-0436, 1998.
- ⁹Ivanov, A. R., "The Effect of the Bluntness and the Half-Angles of a Cone on the Turbulent Transition of a Boundary-Layer at Free-Stream Mach 6," *Uchenye Zapiski*, Vol. 15, No. 3, pp.132-135, 1984 (in Russian).
- ¹⁰McDevitt, J. B., and Mellenthin, J. A., "Upwash patterns on Ablating and Nonablating Cones at Hypersonic Speeds," NASA TN D-5346, 1969.
- ¹¹Meier, H. U., and Kreplin, H., "Experimental Investigation of the Boundary Layer Transition and Separation on a Body of Revolution," *Zeitschrift für Flugwissenschaften und Weltraum-Forschung*, Vol. 4, No. 2, 1980, pp. 65-71.
- ¹²Spall, R. E., and Malik, M. R., "Linear Stability of Three-Dimensional Boundary Layers over Axisymmetric Bodies at Incidence," *AIAA Journal*, Vol. 30, No. 4, 1992, pp. 905-913.
- ¹³Radeztsky, R. H., Reibert M. S., Saric W. S., and Takagi, S., "Effect of Micron-Sized Roughness on Transition in Swept-Wing Flows," AIAA paper 93-0076, 1993.
- ¹⁴Oguni, Y., Nakamura, S., Hosoe, N., and Kawamoto, I., "The Evaluation of Flow Characteristics of 2m x 2m Transonic Wind Tunnel," *Proceedings of the 94th Meeting of Supersonic Tunnel Association, International*, Bromma, Sweden, 2000.
- ¹⁵Koyama, T., and Tsuda, S., "Measurement of Heat Transfer Distribution by Infrared Thermography Technology," *Journal of the Visualization Society of Japan*, Vol. 19, No. 75, 1999, pp.267-272.
- ¹⁶Takaki, R., Iwamiya, T., and Aoki, A., "CFD Analysis Applied to the Supersonic Research Airplane," *Proceedings of the 1st International CFD Workshop for Supersonic Transport Design*, National Aerospace Lab., Tokyo, 1998, pp. 68-72.
- ¹⁷Owen, F. K., "Transition Experiments on a Flat Plate at Subsonic and Supersonic Speeds," *AIAA Journal*, Vol. 8, No. 3, 1970, pp. 518-523.
- ¹⁸Townsend, A. A., "Momentum and energy diffusion in the turbulent wake of a cylinder," *Proceedings of the Royal Society of London, Series A*, Vol. 197, No. A1048, 1949, pp. 124-140.
- ¹⁹Yoshida, K., Ueda, Y., Sugiura, H., Tokugawa, N., Atobe, T., Arnal, D., Archamboud, J. P., and Seraudie, A., "Boundary Layer Transition Analysis on NEXST-1 Airplane: NAL-ONERA Cooperative Research Project," *Proceedings of the 3rd International Workshop on Supersonic Civil Aircraft*, National Aerospace Lab., Tokyo, 2001, pp. 1.
- ²⁰Charters, A. C., "Transition between Laminar and Turbulent Flow by Transverse Contamination," NACA TN-891, 1943.
- ²¹Bippes, H., Muller, B., and Wagner, M., "Measurements and Stability Calculations of the Disturbance Growth in an Unstable Three-Dimensional Boundary Layer," *Physics of Fluids A*, Vol. 3, No. 10, 1991, pp. 2371-2377.

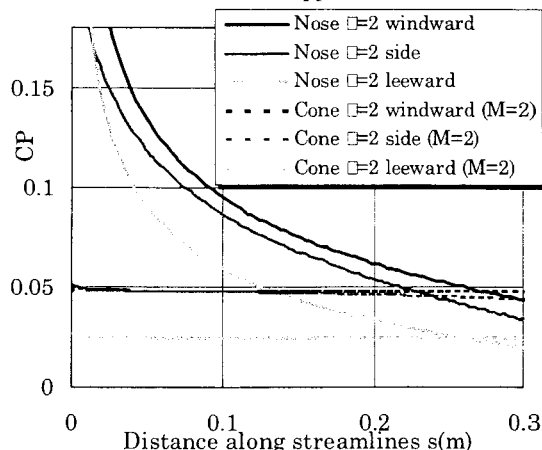


Fig. 1a Comparison of pressure distributions of the model

with those of 10 deg cone.

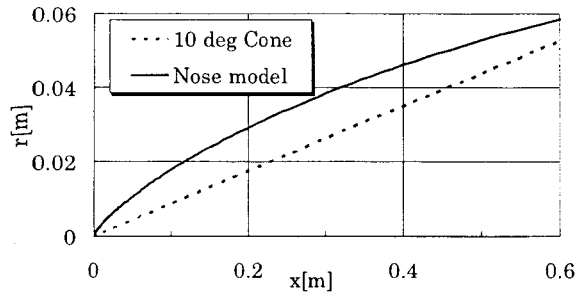


Fig. 1b Comparison of the model configuration with the 10 deg cone.

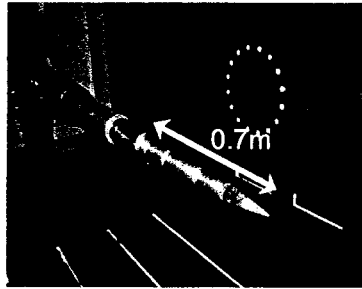


Fig. 2 Axisymmetric nose model.

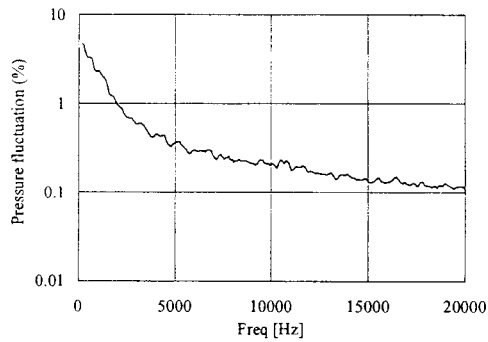


Fig. 3 Power spectrum of the pressure fluctuation in the JAX 2m transonic wind tunnel.

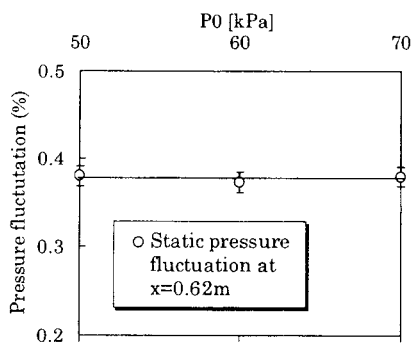


Fig.4a Effect of total pressure on static pressure fluctuation on the model.

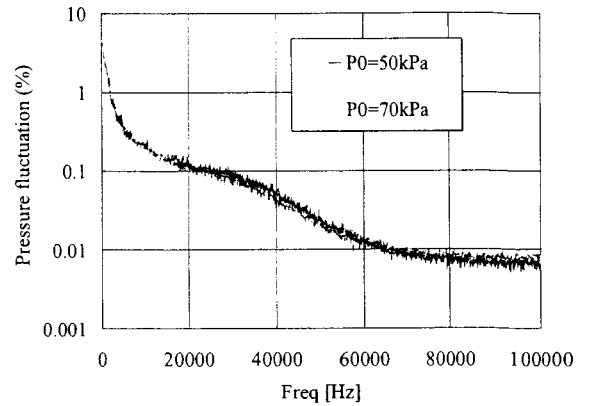


Fig. 4b Effect of total pressure on the power-spectrum of the static pressure fluctuation.

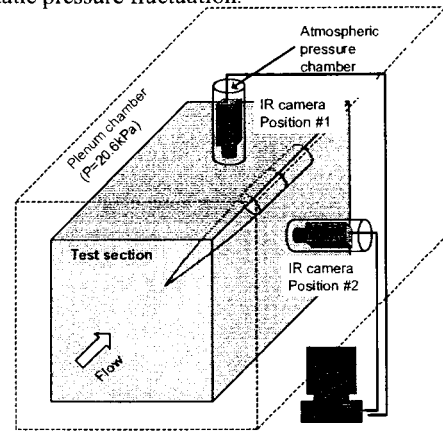


Fig. 5 Infrared camera setup

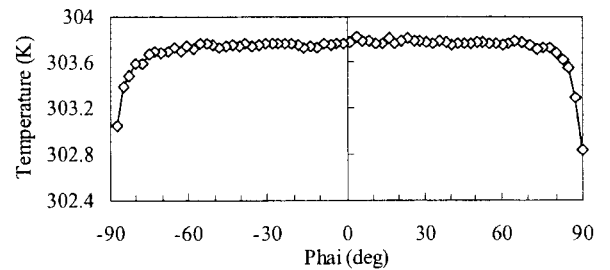


Fig. 6a Circumferential distribution of surface temperature at 0-deg AOA.

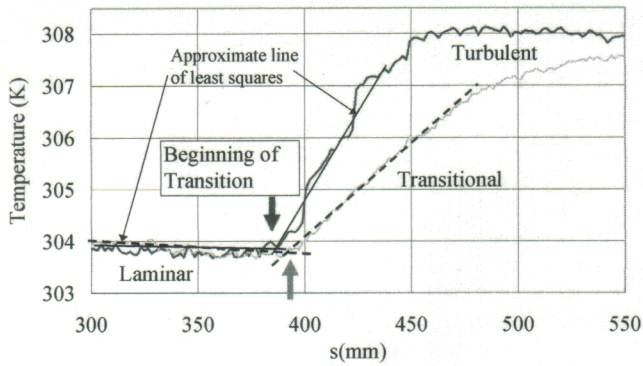


Fig. 7 Examples of temperature profiles measured using IR camera.

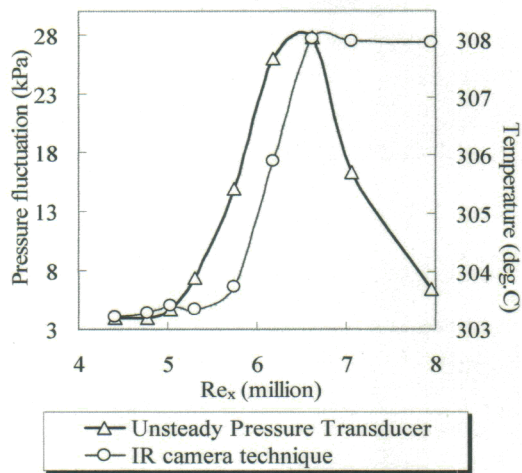


Fig. 8 Comparison between surface temperature and pressure fluctuation at $x=0.62m$ on the windward ray.

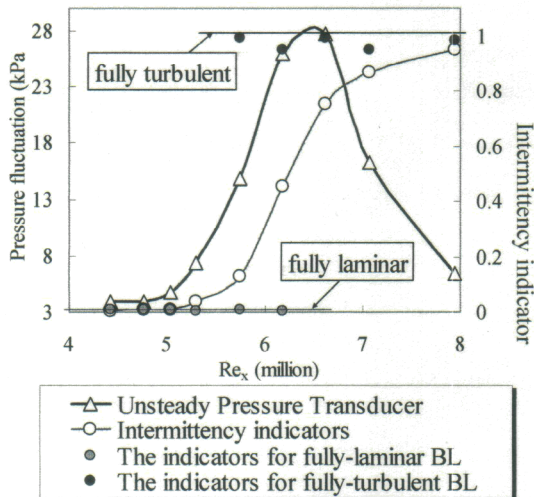


Fig. 9 Comparison between intermittency and magnitude of surface pressure fluctuation at $x=0.62m$ on the windward ray.

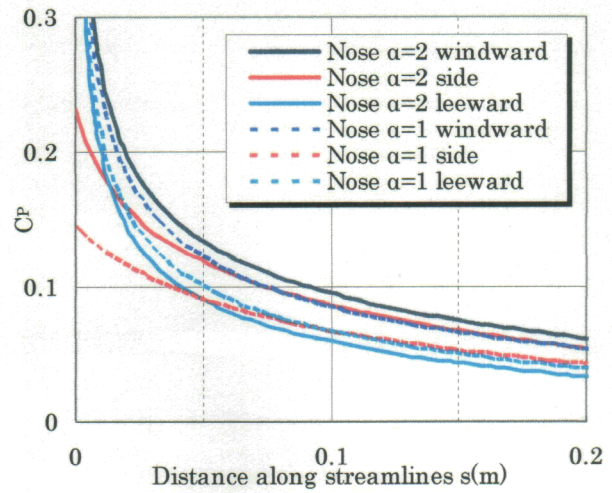


Fig. 10 Comparisons between the measured and the calculated pressure distributions at 1- and 2- deg AOA.

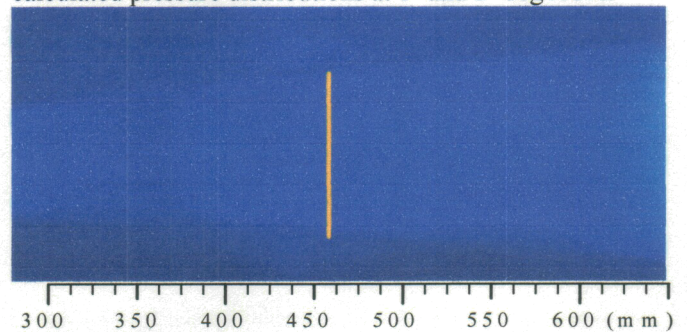


Fig. 11a Side view of surface temperature distribution at 0-deg AOA.

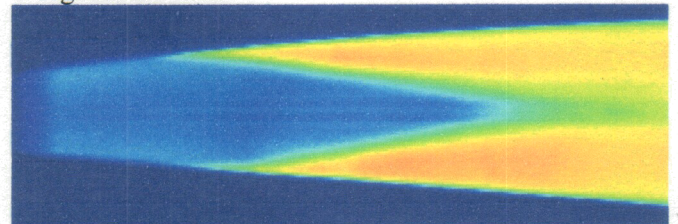


Fig. 11b Top view of surface temperature distribution at 2-deg AOA.

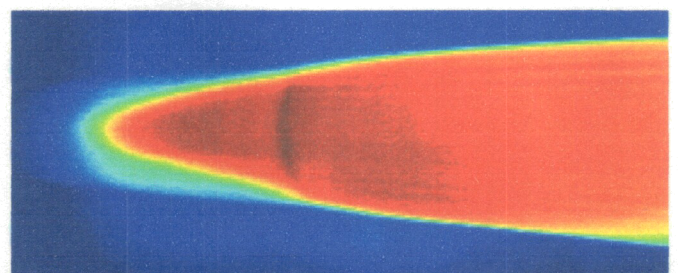


Fig. 11c Side view of surface temperature distribution at 2-deg AOA.

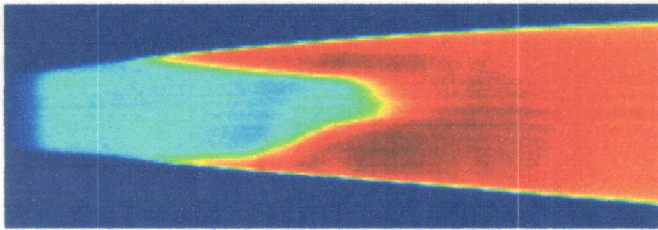


Fig. 11d Bottom view of surface temperature distribution at 2-deg AOA.

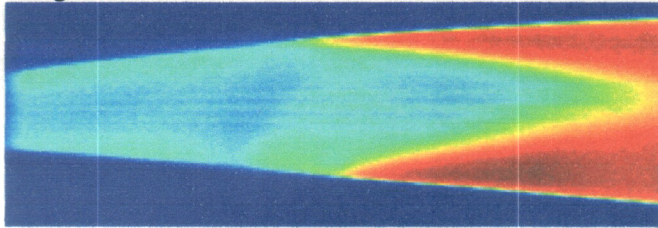


Fig. 11e Top view of surface temperature distribution at 1-deg AOA.

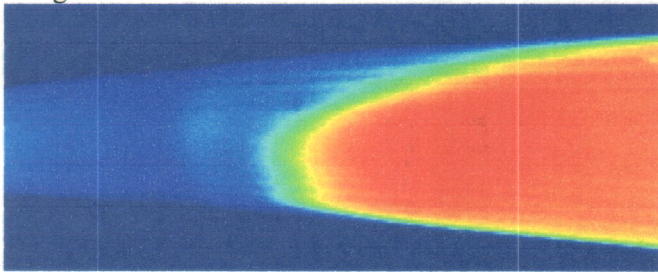


Fig. 11f Side view of surface temperature distribution at 1-deg AOA.

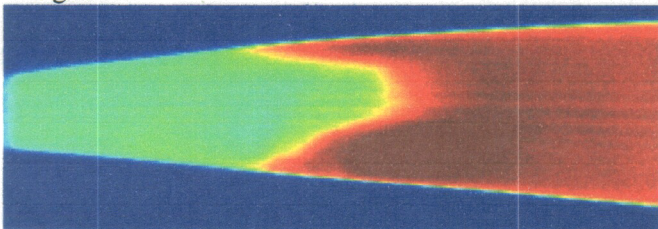


Fig. 11g Bottom view of surface temperature distribution at 1-deg AOA.

303 304 305 306 307 308 (K)

Fig. 11g Bottom view of surface temperature distribution at 1-deg AOA.

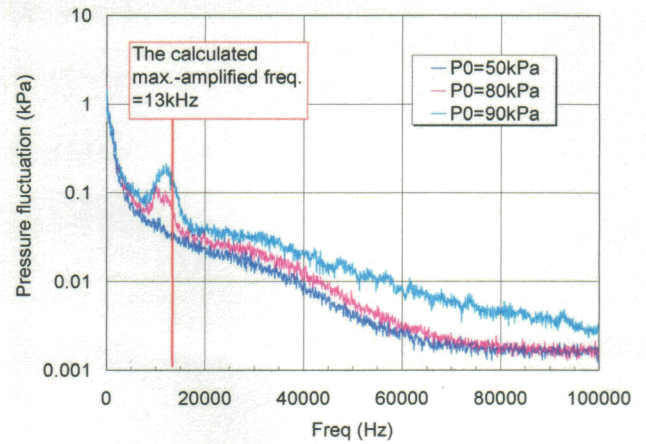


Fig. 12a Power spectrum at $x=0.62m$ at 0-deg AOA.

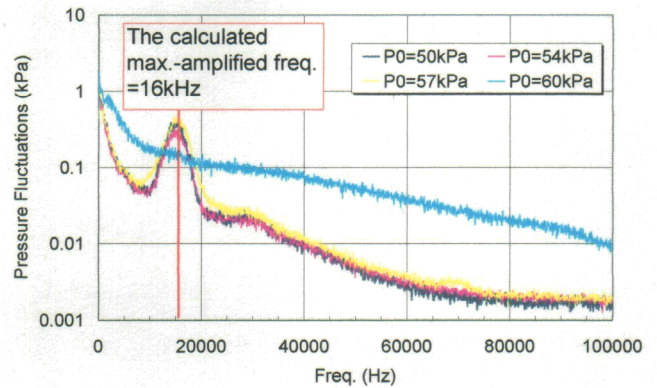


Fig. 12b Power spectrum at $x=0.62m$ on the windward ray at 2-deg AOA.

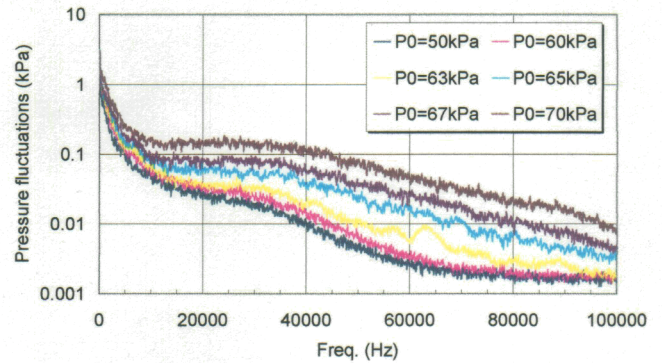


Fig. 12c Power spectrum at $x=0.62m$ on the leeward ray at 2-deg AOA.

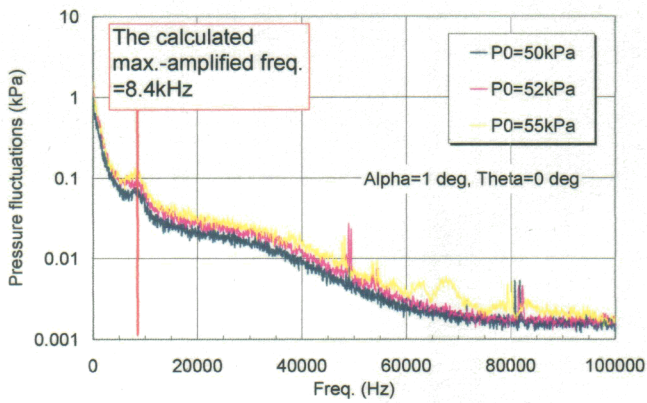


Fig. 12d Power spectrum at $x=0.62m$ on the leeward ray at 1-deg AOA.

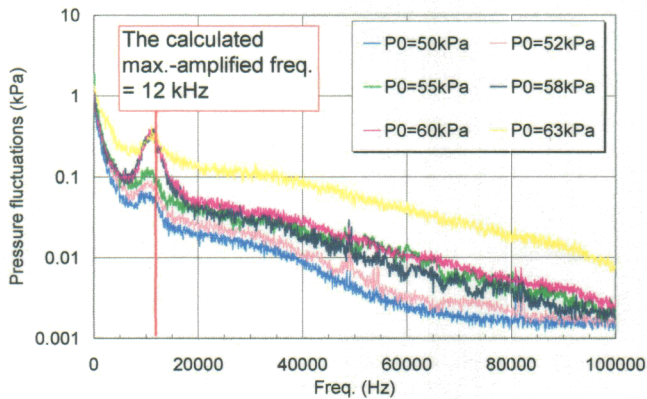


Fig. 12e Power spectrum at $x=0.62m$ and $\theta=90$ deg at 1-deg AOA.

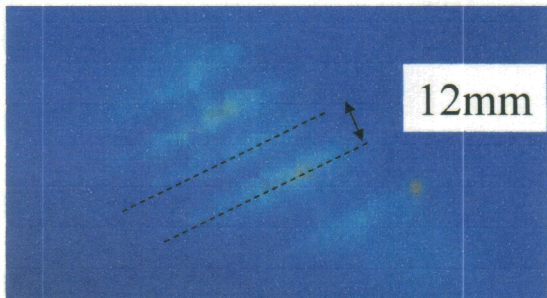


Fig. 13 Enlarged view of surface temperature distribution near $x=0.62m$ and $\theta=90$ deg.

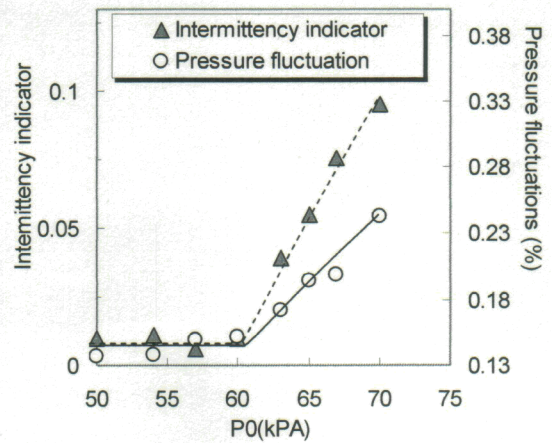
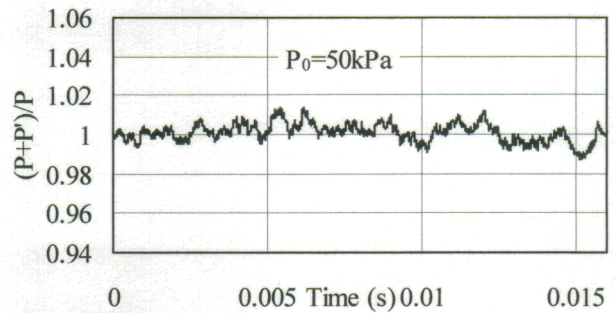
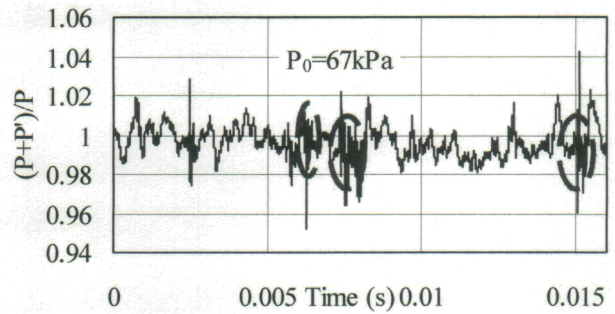


Fig. 14 Comparison between intermittency and magnitude of pressure fluctuation at $x=0.62m$ on the leeward ray.



a) At $P_0=50kPa$.



b) At $P_0=67kPa$

Fig. 15 Pressure fluctuation at $x=0.62m$ on the leeward ray.